Generation and Propagation of Superhigh-Frequency Bulk Acoustic Waves in GaAs

Diego H.O. Machado,[1,2] Antonio Crespo-Poveda●,[1,*] Alexander S. Kuznetsov,[1] Klaus Biermann,[1] Luis V.A. Scalvi●,[2] and Paulo V. Santos[1,†]

[1]*Paul-Drude-Institut für Festkörperelektronik, Leibniz-Institut im Forschungsverbund Berlin e.V., Hausvogteiplatz 5–7, 10117 Berlin, Germany*

[2]*Department of Physics, São Paulo State University (UNESP), School of Sciences, and Graduate Program in Materials Science and Technology (POSMAT), Av. Eng. Luiz Edmundo C. Coube 14-01, 17033-360 Bauru, SP, Brazil*

Coherent superhigh-frequency (SHF) vibrations provide an excellent tool for the modulation and control of excitations in semiconductors. Here, we investigate the piezoelectric generation and propagation of longitudinal bulk acoustic waves (LBAWs) with frequencies up to 20 GHz in GaAs crystals using bulk acoustic-wave resonators (BAWRs) based on piezoelectric thin ZnO films. We show that the electro-acoustic conversion efficiency of the BAWRs depends sensitively on the sputtering conditions of the ZnO films. The BAWRs are then used for the study of the propagation properties of the LBAWs in GaAs in the frequency and temperature ranges from 1 to 20 GHz and 10 and 300 K, respectively, which have so far not been experimentally accessed. We find that the acoustic absorption of GaAs in the temperature range from 80 K to 300 K is dominated by scattering with thermal phonons. In contrast, at lower temperatures, the acoustic absorption saturates at a frequency-dependent value. Experiments carried out with different propagation lengths indicate that the saturation is associated with losses during reflections at the sample boundaries. We also demonstrate devices with a high quality factor fabricated on top of acoustic Bragg reflectors. The results presented here prove the feasibility of high-quality acoustic resonators embedding GaAs-based nanostructures, thus opening the way for the modulation and control of their properties by electrically excited SHF LBAWs.

I. INTRODUCTION

Acoustoelectric devices find applications in different areas, including signal processing, sensorics, as well as acoustooptic and acoustoelectric modulation. Several recent studies have demonstrated that acoustic waves are an excellent tool for the manipulation and control of optoelectronic excitations in these structures (for a recent review, see Ref. [1]). Both surface and bulk acoustic vibrations can be electrically excited by applying a microwave electromagnetic field to a piezoelectric material. Surface acoustic waves (SAWs) are normally generated by applying the field via interdigitated transducers deposited on a piezoelectric surface [2]. Bulk acoustic waves (BAWs) can be conveniently generated by bulk acoustic-wave resonators (BAWRs) consisting of a piezoelectric layer sandwiched between two metallic contacts, as illustrated in Fig. 1(a) [3,4].

The past two decades have witnessed significant efforts to increase the operation frequency of electroacoustic devices to the superhigh-frequency (SHF) range extending from 3 to 30 GHz. Here, one of the motivations has been the opening of new high-frequency bands for mobile telecommunication, generating a demand for filters in the range of a few gigahertz. Operation at high frequencies also increases the sensitivity of electroacoustic sensors and improves the time response of optomechanical structures as well as acousto-optic modulators. For the above applications, leakage of the vibration induced in the piezoelectric layer into the substrate is undesirable. Therefore, the BAWRs are normally fabricated on a suspended membrane (these structures are normally known as thin-film bulk acoustic resonators, FBARs) or on a layer stack designed as an acoustic reflector, thus forming a solidly mounted resonator (SMR).

The availability of electrically excited and coherent SHF vibrations also opens the way for novel functionalities. Vibrations interact with a wide range of electronic and magnetic transitions in solid matter: some of these transitions with present technological relevance

_____

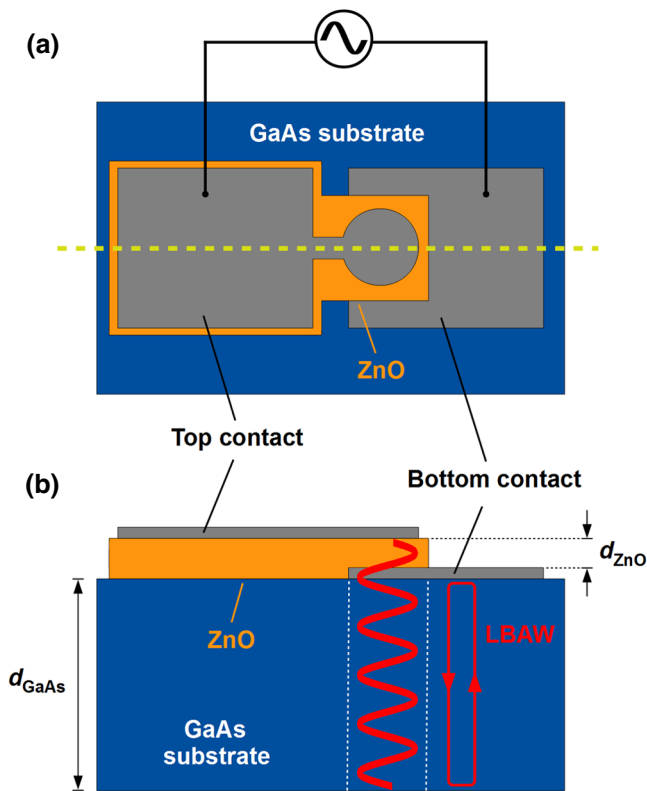[*]poveda@pdi-berlin.de
[†]santos@pdi-berlin.de

FIG. 1. A BAWR for the generation of superhigh-frequency longitudinal bulk acoustic waves (LBAWs) based on a piezoelectric ZnO thin film of thickness d_{ZnO}. (a) A top view, showing the metal contacts. (b) A cross section along the horizonal dashed line in (a). LBAW generation takes place in the overlapping area of the metal contacts, which is delimited by the vertical dashed lines. d_{GaAs} denotes the thickness of the GaAs substrate.

lie in the SHF range. Examples are the quantum levels of nanomechanical oscillators [5,6], superconducting quantum bits [7,8], quantum dots [9,10], two-level single-photon emission centers [11,12], and magnetic excitations [13]. Furthermore, vibrations with frequencies above 3 GHz have equivalent temperatures that exceed the temperatures presently achieved in low-temperature refrigerators (down to 10 mK), thus opening a way for the isolation and manipulation of single vibration quanta.

Several groups have demonstrated the piezoelectric generation of LBAWs with frequencies between 10 GHz and 20 GHz [14–17]. In most of these cases, the structures consist of AlN-based FBARs or SMRs on acoustic reflectors fabricated on a silicon or diamond substrate. In parallel to the developments on BAWRs, the piezoelectrical excitation of SAWs has been extended to frequencies up to 32 GHz in GaAs crystals [18] and up to 24 GHz in silicon crystals coated with a piezoelectric ZnO film [19].

The optoelectronic properties together with the mature technology for the growth of high-quality nanostructures

make (In,Al,Ga)As alloys a relevant material system for nanomechanical science and technology. Consequently, techniques for the generation of LBAWs in these materials as well as the precise knowledge of their propagation properties become key issues for the realization of acoustic resonators with a high quality factor Q. Despite the technological significance of (In,Al,Ga)As alloys, experimental data on the propagation of SHF acoustic waves in GaAs remain very scarce. In particular, there is a gap in the experimental determination of the acoustic absorption between the subgigahertz range probed by ultrasonic propagation [20] and the frequency range starting at about 50 GHz [21–24], which is normally accessed using laser acoustics (see, e.g., the compilation of experimental results summarized in Fig. 3 of Ref. [24]).

In this paper, we investigate the electric generation and propagation of SHF LBAWs in GaAs crystals using BAWRs of the type illustrated in Fig. 1(a). These structures require a piezoelectric thin film: as previously mentioned, both textured ZnO and AlN can be used for this purpose. AlN is better suited for high-frequency BAWRs due to the higher acoustic velocity and compatibility with the silicon complementary metal-oxide semiconductor (CMOS) technology [25]. The elastic properties of ZnO, in contrast, are better matched to those of (Al,Ga)As alloys, which is a favorable property for SAW applications in particular. In the initial stages of this work, we have fabricated BAWRs using both textured AlN [26] and ZnO layers deposited on GaAs by sputtering. We found that both types of films lead to comparable BAWR performances up to frequencies of at least 10 GHz. In the present studies, we concentrate on BAWRs fabricated using sputtered ZnO films. The remaining sections of the paper are organized as follows. The procedures used for the fabrication of these BAWRs, including the fabrication steps for the deposition of contacts sandwiching the piezoelectric ZnO layers, are described in Sec. II. The experimental results are presented in Sec. III. Here, we first address the deposition of high-quality piezoelectric layers (Sec. III A) and then proceed to the analysis of the electrical response of SHF BAWRs deposited on bare GaAs substrates (Sec. III B) as a function of frequency and temperature (Sec. III D). These studies are then extended, in Sec. III E, to structures fabricated on acoustic Bragg reflectors grown epitaxially on GaAs substrates. The BAWRs are then employed for the study of LBAW propagation in GaAs over a wide range of frequencies and temperatures. Section IV is devoted to the mechanisms responsible for the acoustic absorption. Here, we first identify the different mechanisms leading to acoustic absorption (Sec. IV A). Their behavior at room and cryogenic temperatures is then addressed in Secs. IV B and IV C, respectively. Finally, the main results of the paper are summarized in Sec. V.

II. EXPERIMENTAL DETAILS

A. BAW transducer design

To a first approximation, the central resonance frequency of the BAWRs of Fig. 1 is given by the following equation:

$$f_R \cong \frac{v_{ZnO}}{2d_{ZnO}}. \tag{1}$$

Here, $v_{ZnO} = 6070$ m/s is the propagation velocity of the LBAWs in the ZnO film [27] and d_{ZnO} is its thickness. The previous approximation for the resonance frequency neglects the influence of the metal contacts on the resonant modes and, thus, strictly applies only for structures with thick piezoelectric layers. In order to obtain more reliable results, we carry out numerical simulations of the frequency dependence of the excited BAWs using a finite-element method [28,29]. The simulations are performed by exciting the BAWR with radio-frequency (rf) voltages of different frequencies and solving the coupled piezoelectric and mechanical equations to determine the spatial distribution of the acoustic field as well as the electric power converted to the acoustic modes. In the calculations, we use the lateral dimensions as well as the nominal thicknesses of the ZnO layers and metal contacts of the fabricated samples (see the caption of Fig. 2). The thickness of the GaAs substrate, in contrast, is set to 5 μm to limit the calculation time. In order to minimize acoustic reflections, the lateral and bottom sides of the calculation domain are surrounded by perfectly matched layers (PMLs).
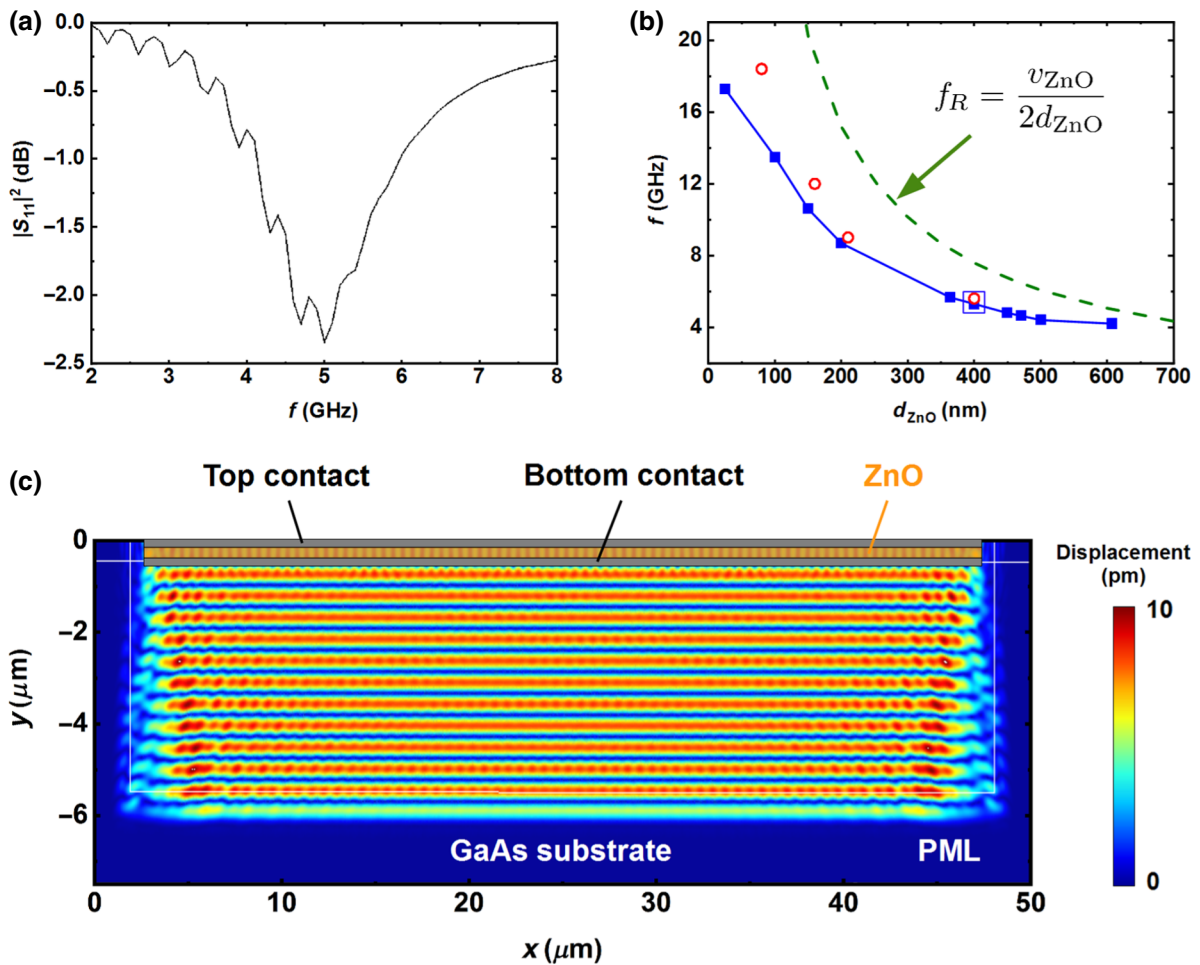

FIG. 2. (a) The calculated dependence of the $|s_{11}|^2$ scattering parameter (corresponding to the rf reflection coefficient) for a BAWR on a GaAs (001) wafer consisting of a $d_{ZnO} = 440$-nm-thick ZnO layer sandwiched between bottom and top metal contacts formed by a 40-nm Au film and a 10-nm/30-nm/10-nm Ti/Al/Ti layer stack, respectively. The active area of the resonator is equal to 1960 μm^2. (b) The dependence of the resonance frequency on d_{ZnO}: the joined full square symbols are finite-element-method calculations and the open circle symbols are experimental values. The dashed line reproduces the approximation for the resonance frequency given by Eq. (1). The blue open square at $f_R \cong 5$ GHz corresponds to the device simulated in (a) and (c). (c) A cross-section map of the amplitude of the displacement field of the BAWR in (a) at the resonance frequency. The calculation domain is surrounded by perfectly matched layers (PMLs) to reduce acoustic reflections from the sample boundaries.

Figure 2(a) displays the rf scattering parameter s_{11} calculated for a BAWR with a 440-nm-thick ZnO layer and an area of 1960 μm^2 (corresponding to a circular top-contact diameter of 25 μm). s_{11} quantifies the fraction of the electric power reflected by the BAWR. The pronounced dip centered around the resonance frequency $f_R = 5$ GHz arises from the reduced electric reflection as the electrical input drive is converted to an acoustic mode. The oscillations superimposed on the curve are interference fringes due to residual reflections at the back PML. Figure 2(b) displays the calculated (full square symbols) as well as the measured (open circle symbols; see Sec. III C for details) dependence of f_R on the thickness of the ZnO film. The dashed line reproduces the simple first-order approximation for the resonance frequency obtained from Eq. (1). This approximation considerably overestimates the resonance frequency, in particular for structures with thin ZnO layers and, thus, high resonance frequencies. Finally, Fig. 2(c) shows the spatial distribution of the acoustic displacement field $|u|$ in the resonator in Fig. 2(a) as determined for a fixed phase of the applied rf voltage. The stripes on the cross section of the device correspond to the acoustic wave fronts, which are separated by half of the LBAW period.

B. BAWR fabrication

The BAWRs of Fig. 1(a) are deposited on nominally intrinsic GaAs (001) wafers (Wafer Technology Ltd.) with a resistivity $>5.9 \times 10^7$ Ω cm and a Hall mobility >5100 cm^2/(V s). The wafers are double-side polished, with a thickness $d_{GaAs} = (356 \pm 8)$ μm. The bottom contact of the BAWRs consists of a 30-nm-thick Au film deposited on a 10-nm-thick Ti adhesion layer. The metal films are deposited via electron-beam evaporation while the ZnO film is fabricated by rf magnetron sputtering.

The piezoelectric properties of the textured ZnO thin films rely on the preferential orientation of the hexagonal c axis along the direction perpendicular to the surface, which can be controlled by a proper selection of the sputtering conditions and underlying substrate. Au is employed as the back contact due to its favorable impact on the nucleation of the textured ZnO films, a necessary condition for high piezoelectric coupling [30,31]. The sputtering process is carried out in a high-vacuum chamber (base pressure $<10^{-6}$ mbar) with a 5-in. ZnO target placed 8 cm above the sample. The sputtering atmosphere consists of an 80:20 Ar-O$_2$ gas mixture (pressure of 5×10^{-3} mbar). The extra O$_2$ atmosphere ensures the formation of high-resistivity stoichiometric films. The rf sputtering powers are typically of about 100 W. As will be discussed in detail below, the structural and piezoelectric properties of the ZnO films are very sensitive to the sputtering conditions.

Two different approaches are used to define the lateral dimensions of the BAWR layers. The first is a conventional

photolithographic process combining the lift-off deposition of the metallic contact layers with the wet-chemical etching of the sputtered ZnO film. In the second approach, the dimensions of the bottom contact as well as of the ZnO film are defined via evaporation and sputtering, respectively, through shadow masks. For that purpose, we use mechanically machined shadow masks fabricated on a boron-nitride plate, with minimum opening dimensions of approximately 100 μm. The top contact, which defines the active area of the BAWRs, is fabricated by optical lithography.

Figure 3 displays optical micrographs of the two types of structures, indicating the contact areas (top and bottom contacts) as well as the piezoelectric ZnO film. In each case, the dashed red circle indicates the active area of the BAWRs. The main advantage of the shadow mask approach is the simplicity of fabrication, since it has fewer photolithographic steps and does not require the etching of the ZnO layers. The drawbacks of the shadow-mask deposition method are the alignment tolerances ($\simeq 40$ μm) as well as the edge roughness of the layers [cf. Fig. 3(b)] resulting from the mechanical machining of the shadow masks, which are significantly larger than for photolithography. The photolithographic fabrication of the top contact together with a careful alignment to the underlying layers enable the fabrication of structures with active-region dimensions down to approximately 10 μm.
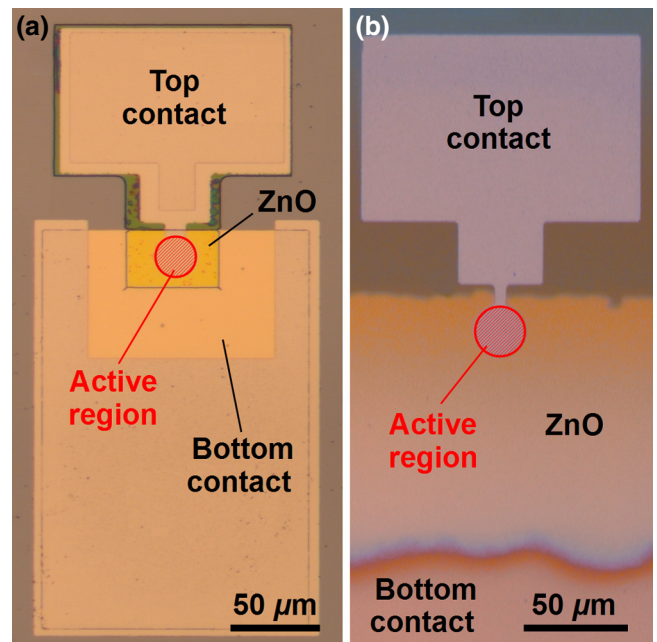

FIG. 3.   Optical micrographs of BAWRs fabricated using (a) optical lithography and (b) shadow-mask deposition. The active area of the BAWRs, where the top and bottom contacts sandwich the piezoelectric ZnO thin film, is indicated by a dashed red circle.

C. Characterization techniques

The structural properties of the BAWR layers are probed using atomic force microscopy (AFM). Their electrical response is investigated using a vector-network analyzer to record the frequency dependence of the rf scattering (s) parameters. The studies are carried out in a low-temperature probe station (temperatures from 10 K to room temperature) with rf tips for contacting the BAWR devices. The setup has also calibration standards for the *in situ* calibration of the scattering parameters.

III. RESULTS

A. Structural properties of the ZnO films

The calculations of Sec. II A [cf. Fig. 2(b)] show that high-frequency (> 10 GHz) BAWRs require ZnO layers with thicknesses below 100 nm. These layers should be smooth, highly resistive, continuous (i.e., without pinholes), and with good piezoelectric properties.

The structural and piezoelectric properties of the ZnO layers depend critically on the deposition conditions. The left-hand panels in Fig. 4 compare AFM micrograph maps of the vertical displacement δz recorded on the surface of BAWRs with 200-nm-thick ZnO films sputtered at different temperatures T_d. The right-hand panels display linear profiles of δz recorded along the dashed lines indicated in the left-hand panels.

Films deposited at room temperature [cf. Fig. 4(f)] have an average surface roughness $r_a \sim 2$ nm [corresponding to the root-mean-square (rms) fluctuation of δz averaged over the area of the micrograph]. For comparison, similar measurements on ZnO films deposited directly on the GaAs (001) surface yield an r_a value of only 0.5 nm. The same applies to the surface of the Au/Ti back contact used as the substrate for ZnO deposition, which has a roughness $r_a = 0.6$ nm, only marginally larger than that of the GaAs substrates. The pronounced roughness of the BAWR surface is attributed to the columnar character of the textured ZnO layers, which is also a necessary condition for piezoelectricity. The surface roughness increases with T_d [cf. Figs. 4(d) and 4(e)]. In addition, the δz profiles of films deposited at high temperatures ($T_d \geq 100\,°C$) exhibit sub-μ hillocks, which lead to spikes in δz with amplitudes exceeding 20 nm. The mechanism for the appearance of these features is not further investigated.

The deposition temperature of the ZnO films has a direct impact on the piezoelectric response of the BAWRs. Figure 5 compares the time-gated rf reflection coefficient $\left|\Delta s^t_{11,1}\right|$ of BAWR structures designed for a resonance frequency $f_R = 5$ GHz with piezoelectric ZnO layers sputtered at different temperatures T_d. As will become clear in Sec. III C, $\left|\Delta s^t_{11,1}\right|^2$ is proportional to the electroacoustic generation efficiency, thus being a figure of merit for the quality of the resonators. The electroacoustic performance
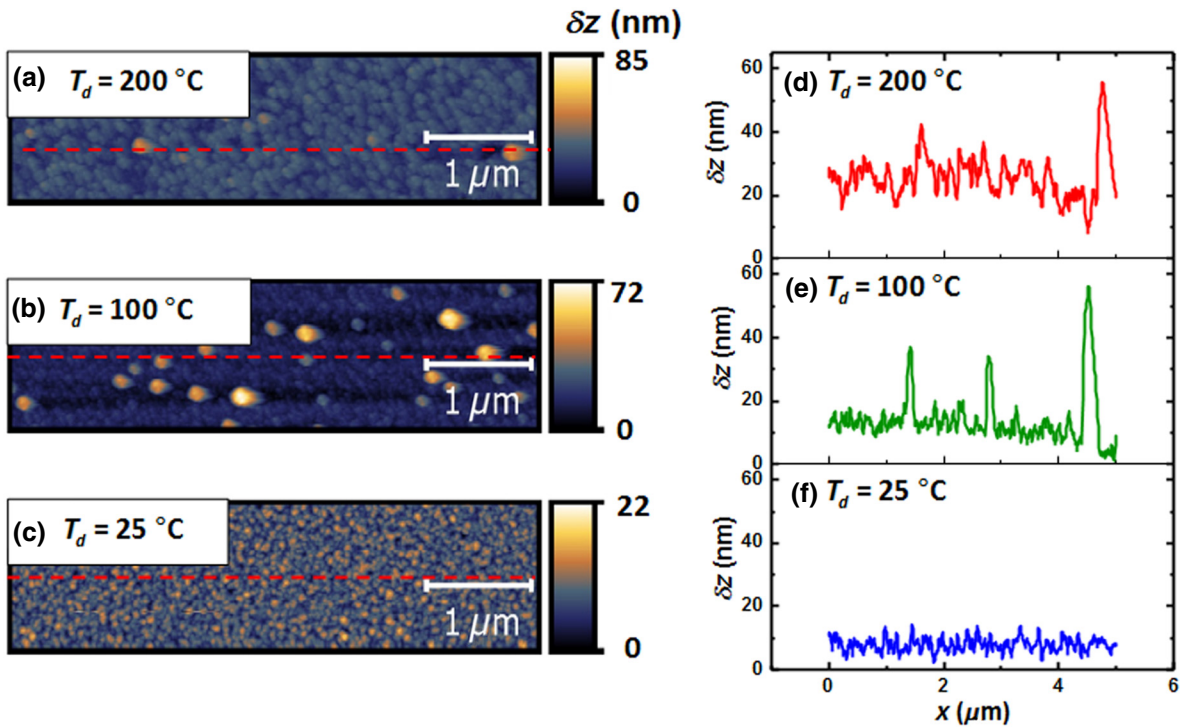

FIG. 4. Atomic force micrographs (AFM) (left-hand panels) and line profiles of the surface displacement (δz, right-hand panels) of BAWRs fabricated using 200-nm-thick piezoelectric ZnO layers sputtered at temperatures (a)–(d) $T_d = 200\,°C$, (b)–(e) $T_d = 100\,°C$, and (c)–(f) $T_d = 25\,°C$. The line profiles are recorded along the dashed lines indicated in the left-hand panels.
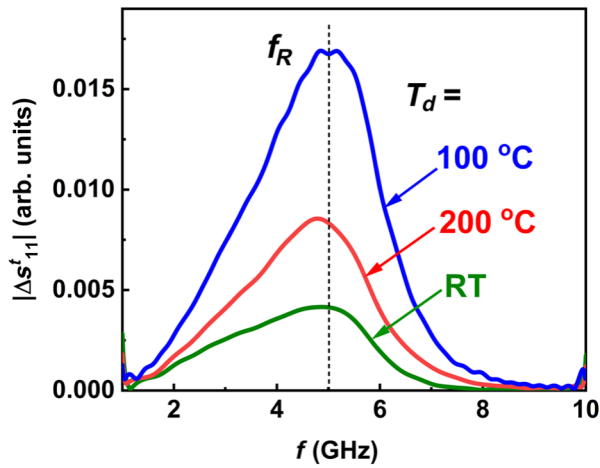
FIG. 5. The dependence of the time-gated $|\Delta s_{11,1}^t|$ response of BAWRs with piezoelectric ZnO layers sputtered at different temperatures T_d. The BAWRs have an active area of 1960 μm^2 and ZnO layers with a thickness of 440 nm. Here, f_R indicates the resonance frequency.

improves considerably when the deposition temperature is increased from room temperature to 100 °C. This result is in agreement with previous studies of piezoelectric ZnO films for the excitation of SAWs on Si [19] and GaAs [31], which show that the film properties improve with the sputtering temperature (in those cases, the sputtering process was carried out at temperatures between 300 and 350 °C). A further increase of the sputtering temperature of the ZnO films on Au to 200 °C results, however, in rougher surfaces (cf. Fig. 4) as well as in a lower fabrication yield with a larger fraction of short-circuited BAWRs. The latter indicates that the higher sputtering temperatures also induce the formation of pinholes. Based on these results, the studies reported in the subsequent sections are carried out using films sputtered at 100 °C, which yield the best electroacoustic performance.

B. Radio-frequency response of BAWRs

Figure 6(a) displays the frequency dependence of the rf reflected power $|s_{11}|^2$ (given in terms of the s_{11} rf scattering parameter) of a BAWR with a 440-nm-thick ZnO layer. The broad dip in the spectrum centered at approximately 5.55 GHz is attributed to the excitation of LBAWs: this resonance frequency corresponds closely to that calculated for the used ZnO thickness in Fig. 2(b). The spectrum also shows a series of oscillations (cf. the figure inset), which are attributed to Fabry-Perot fringes induced by reflections of the LBAW at the back surface of the GaAs substrate (see details below). The 6.71-MHz period of the oscillations agrees very well with the expected value given by $t_r^{-1} = v_{\text{GaAs}}/(2d_{\text{GaAs}})$, where $d_{\text{GaAs}} = 356$ μm and $v_{\text{GaAs}} = 4731$ m/s denote the thickness and longitudinal acoustic velocity in the GaAs substrate [32], respectively.

The frequency response of the BAWR is modeled using the modified Butterworth–van Dyke (BvD) equivalent electric circuit [33] depicted in Fig. 6(d). Here, the electroacoustic transduction takes place in the rightmost branch, where R_a is the motional resistance quantifying the conversion of electric into acoustic power. The reactive components C_a and L_a are the motional capacitance and inductance, which are proportional to the inverse stiffness and density of the BAWR medium, respectively. The parallel branch includes the electrical capacitance across the electrodes, $C_s = \epsilon_0 \epsilon_{\text{ZnO}} (A_{\text{BAWR}}/d_{\text{ZnO}})$, in series with a resistance R_s, which accounts for dielectric losses. In the previous expression for C_s, A_{BAWR} is the effective area of the BAWR and $\epsilon_0 \epsilon_{\text{ZnO}}$ the permittivity of the piezoelectric material. The BAWR components are connected to an rf source V_{rf} with an internal series impedance $Z_0 = 50$ Ω.

The lumped components R_s, R_a, C_a, and L_a are determined by fitting the frequency response of the Butterworth–van Dyke circuit to the measured $|s_{11}|^2$ spectrum. The shunt capacitance C_s is also fitted in order to account for small variations in the thickness and dimensions of the BAWR. The solid line marked "BvD" in Fig. 6(a) displays the filter response calculated using the fitted values for the components listed in the caption. The BvD model reproduces the measured resonance dip at the resonance frequency, $f_R = 1/(2\pi \sqrt{L_a C_a})$, reasonably well. The dashed line "R_s-C_s" shows, for comparison, the response of the R_s-C_s parallel branch in the circuit of Fig. 6(d), which accounts for the dielectric losses of the BAWR.

The curve marked "BvD" in Fig. 6(c) displays the spectral dependence of the effective conversion efficiency $\Delta |s_{11}|^2$ obtained from the difference between the dashed and solid curves in Fig. 6(a). The highest conversion value of $\Delta |s_{11}|^2 \sim 0.35$ at the resonance frequency is mainly limited by the high acoustic impedance R_a (approximately 250 Ω for the present structure), which considerably exceeds the characteristic impedance $Z_0 = 50$ Ω.

C. BAWR transduction efficiency

The analysis based on the BvD model of the previous sections yields information about the overall electroacoustic conversion efficiency. In this section, we use rf measurements in the time domain to estimate the fraction of the acoustic power transduced to propagating LBAWs.

The time-domain trace for $|s_{11}|^2$ of Fig. 6(b) shows a series of acoustic echoes, which are associated with the Fabry-Perot oscillations depicted in the inset of Fig. 6(a). This trace is determined by Fourier transforming the frequency response in the frequency range from 3 to 7 GHz. Three echoes at times $i \times t_r$ ($i = 1, 2, 3$), corresponding to multiple round trips across the substrate with the LBAW velocity, can be observed in this case. The inset of Fig. 6(c) shows that the integrated amplitude of
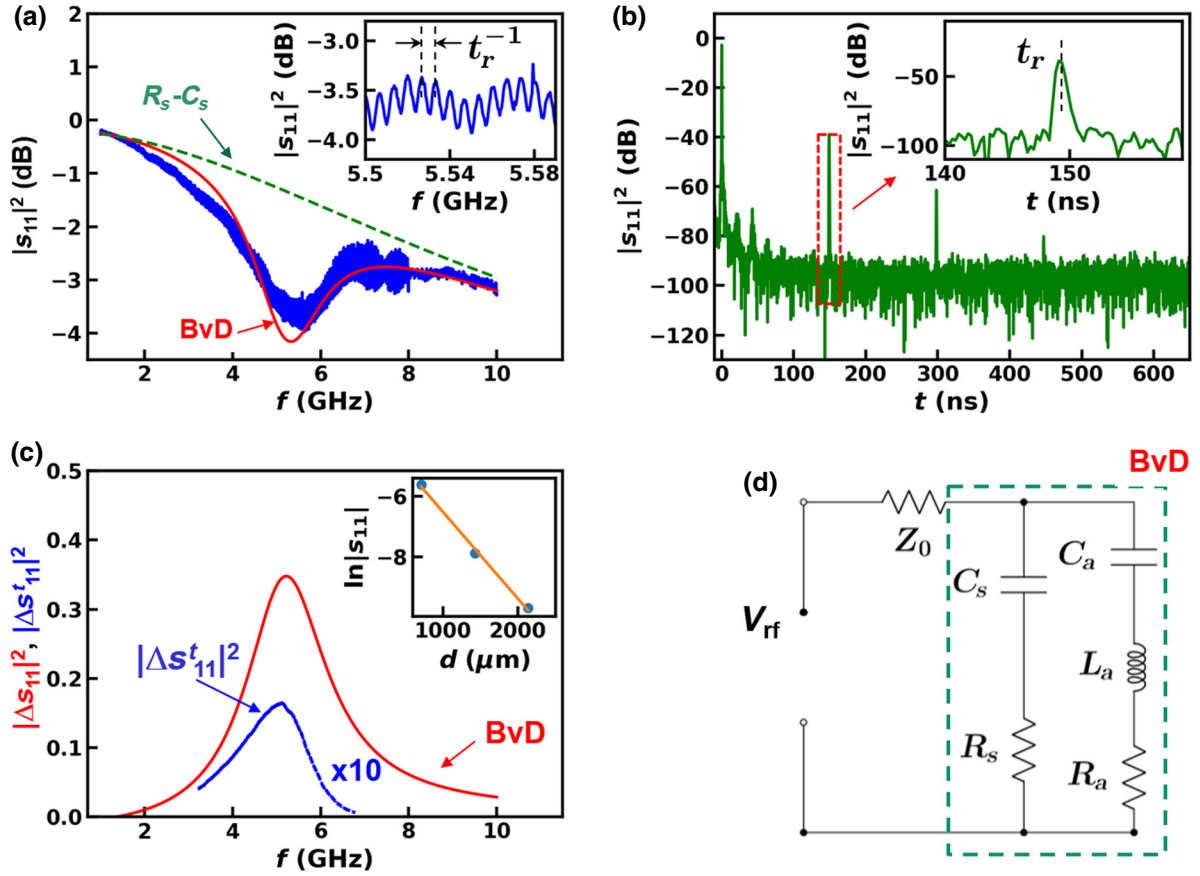
FIG. 6. (a) The frequency dependence of $|s_{11}|^2$ at room temperature for a BAWR with a 440-nm-thick ZnO film. The solid line is a fit to the Butterworth–van Dyke (BvD) circuit model shown in (d), while the dashed line represents the response due to the $C_s - R_s$ shunt branch. The magnified region in the inset shows Fabry-Perot-like oscillations with frequency t_r^{-1}. (b) Time-domain traces for $|s_{11}|^2$ displaying the echoes due to LBAW reflection at the back side of the substrate. The inset displays details of the first echo at time t_r. (c) The effective electroacoustic conversion efficiency $|\Delta s_{11}|^2$ determined from the difference between the curves marked "BvD" and "R_s-C_s" in (a). The line marked "$|\Delta s_{11}^t|^2$" is the rf reflectivity contribution from LBAW modes determined from the intensity of the echoes in (b), which are plotted as a function of the echo-propagation distance d in the inset. (d) The BvD lumped-filter model used to fit the rf spectrum in (a), yielding the following parameters: $R_a = 260\ \Omega$, $R_s = 18\ \Omega$, $C_a = 4.4$ fF, and $L_a = 22$ nH.

the $|s_{11}|^2$ echoes decays exponentially according to $r_{\mathrm{eff}} = \exp(-2\alpha_{\mathrm{eff}} d_{\mathrm{GaAs}})$. Here, d_{GaAs} is the substrate thickness and α_{eff} is the effective acoustic absorption coefficient, defined as the inverse of the LSAW propagation distance for an amplitude decay by a factor of e^{-1} (where e is Euler's number). Note that α_{eff} is an effective coefficient since it includes not only propagation losses but also losses due to scattering at surfaces and interfaces. From the plot, we extract $\alpha_{\mathrm{eff}} = 0.0029\ \mu\mathrm{m}^{-1}$ as well as the exponential amplitude decay factor per round trip across the substrate $r_{\mathrm{eff}} = 0.13$ for 5-GHz LBAWs propagating at room temperature. As will become clear in the subsequent sections, the progressive amplitude decay of the echoes at room temperature is mainly due to acoustic losses during propagation through the substrate.

The effective electric response Δs_{11}^t arising from the electrical reabsorption of the LBAW modes by the BAWR

can be obtained by summing the time-gated contributions from the echoes according to the following equation:

$$\Delta s_{11}^t = \sum_{i=0}^{\infty} s_{11,i}^t \left(e^{2\pi jf\, t_r} r_{\mathrm{eff}}\right)^i = s_{11,0}^t \frac{1}{1 - e^{2\pi jf\, t_r} r_{\mathrm{eff}}}$$

$$= s_{11,1}^t \frac{1}{r_{\mathrm{eff}}\left[1 - e^{2\pi jf\, t_r} r_{\mathrm{eff}}\right]}, \quad \text{with } j = \sqrt{-1}. \quad (2)$$

In this expression, the exponential factor containing the LBAW frequency (f) yields the phase shift accumulated by the wave during a round trip across the substrate. The closed forms on the right-hand side are obtained by using the expression for the summation of a convergent infinite series. For $i > 0$, $s_{11,i}^t$ denotes the component of the frequency response associated with the ith echo in the time-domain traces for s_{11}. These components can be directly

obtained from time-domain traces: this procedure is normally used to discriminate the acoustic response from the much faster electromagnetic one. The total response Δs_{11}^{t} also includes the response $s_{11,0}^{t}$ at short times (i.e., before the LBAW leaves the transducer region), which overlaps with the much stronger electromagnetic reflection at zero times, thus normally remaining inaccessible. The last term on the right-hand side of Eq. (2) shows that the total rf response associated with the LBAW can be retrieved by correcting $s_{11,1}^{t}$ by a factor that depends on r_{eff}.

Δs_{11}^{t} represents the frequency-dependent fraction of the input electrical power, which is transduced to a propagating LBAW mode and subsequently reconverted to an electric signal. The latter requires that the LBAW propagates without wave-front distortions, which can arise from diffraction or reflections on irregular surfaces, since these will reduce the reconversion efficiency to an electrical signal by the BAWR. Δs_{11}^{t} is thus a direct measure of the BAWR transduction efficiency as well as of the ability of the LBAW mode to propagate without absorption and wave-front distortions.

If r_{eff} in Eq. (2) is small, then the amplitude of the Fabry-Perot oscillations in Fig. 6(a) can be approximated by $|\Delta s_{11}^{t}|^2 \sim |s_{11,0}^{t}|^2 [1 + 2r_{\mathrm{eff}} \cos(2\pi f\, t_r)]$. This expression shows that the oscillations are sinusoidal in this approximation, with an amplitude proportional to $2r_{\mathrm{eff}}$. Equation (2) also provides a convenient route to determine the LBAW generation efficiency by high-frequency (> 5 GHz) ZnO/GaAs BAWRs, where the low electroacoustic conversion efficiency leads to small dips in the $|s_{11}|^2$ spectra. Note that, in general, one needs to take into account the frequency dependence of r_{eff}. The latter can, however, be neglected if the time traces are calculated for a small frequency range Δf_R of the s_{11} spectrum around the BAWR resonance.

The line marked $\left|\Delta s_{11}^{t}\right|^2$ in Fig. 6(c) displays the rf reflectivity $\left|\Delta s_{11}^{t}\right|^2$ calculated from Eq. (2) using the frequency-independent $r_{\mathrm{eff}} = 0.13$ determined from the amplitude of the echoes (cf. the inset). The peak position as well as the line shape of the $\left|\Delta s_{11}^{t}\right|^2$ resonance resembles that determined from the fits to the BvD circuit model (solid line). The peak intensity of approximately 1.5% is, however, much lower than the 35% peak value of $|\Delta s_{11}|^2$ obtained by the BvD analysis. We thus conclude that only a small fraction of the electroacoustical power of the propagating LBAW mode is recovered by the transducer.

According to the calculations shown in Fig. 2(b), the resonance frequency f_R of the BAWRs can be increased by reducing the thickness of the piezoelectric layer. This behavior is experimentally confirmed by the dots in this figure, which display the center frequency of the $|s_{11,i}^{t}|^2$ resonances measured at room temperature. While the calculations reproduce the resonance frequencies for large d_{ZnO} very well, the experimental points lie above the

calculations for small ZnO thicknesses. We attribute this discrepancy to slight deviations between the real and nominal thicknesses of the Au/Ti bottom contact in these structures.

D. Temperature dependence of the LBAWR transduction

The dots in Fig. 7(a) display the dependence of the effective absorption coefficient α_{eff} on the frequency, as determined at room temperature by analyzing the amplitude of the $|s_{11}|^2$ echoes for frequency slices $\Delta f_R = 1$ GHz. The increase of the product $d_{\mathrm{ZnO}}\alpha_{\mathrm{eff}}$ with the frequency limits the frequency range for the observation of echoes to approximately 10 GHz (note that the determination of α_{eff} requires at least two echoes in the time-domain traces). This frequency range can be extended considerably by performing the measurements at low temperatures. Figure 7(b) compares the time-domain traces for s_{11} recorded on a structure for $f_R = 12$ GHz at 10 K and 100 K. Note that the intensity and the number of detected echoes increase substantially in the former case, thus indicating a much lower acoustic absorption coefficient α_{eff} at low temperatures. The reduction of α_{eff} is accompanied by a large enhancement of $|\Delta s_{11}^{t}|^2$, as illustrated in Fig. 7(c) for a BAWR with $f_R = 12$ GHz. It is evident that there is an almost tenfold increase of $|\Delta s_{11}^{t}|^2$ as the temperature is decreased from 100 K to 10 K. At low temperatures, it thus becomes possible to detect multiple echoes for LBAWs with frequencies exceeding 20 GHz. As an example, Fig. 7(d) compares $|\Delta s_{11}^{t}|^2$ spectra of BAWRs with ZnO layer thicknesses varying from 80 to 400 nm. The structure with the thinner ZnO layer resonates at 18.4 GHz, with a bandwidth of approximately 5 GHz. We believe that the latter is the highest reported resonance frequency for BAWR on GaAs.

E. BAWRs on distributed Bragg reflectors

The quality factor of BAWRs becomes significantly enhanced when they are deposited on distributed Bragg reflectors (DBR) to prevent wave leakage to the substrate [34–36]. Figures 8(a) and 8(b) compare spectra recorded at 10 K of the scattering ($|s_{11}|^2$) and admittance ($|y_{11}|$) parameters of BAWRs with resonant frequencies f_R of 6.4 GHz and 19.64 GHz, respectively. These BAWRs are deposited on DBRs consisting of $Al_{x_1}Ga_{(1-x_1)}As/Al_{x_2}Ga_{(1-x_2)}As$ layer stacks with different Al contents x_i, each with a thickness corresponding to a quarter of the resonance acoustic wavelength. The DBRs are grown on (100) GaAs substrates using molecular-beam epitaxy. For the $f_R = 6.4$ GHz structure, the DBRs consist of ten stack pairs with Al contents $x_1 = 0$ and $x_2 = 0.85$ and thicknesses of 179 nm and 210 nm, respectively. For the second structure, the DBR has 20 layer pairs with compositions $x_1 = 0.05$ and $x_2 = 0.85$ and corresponding thicknesses of 59.7 nm and 70 nm, respectively.
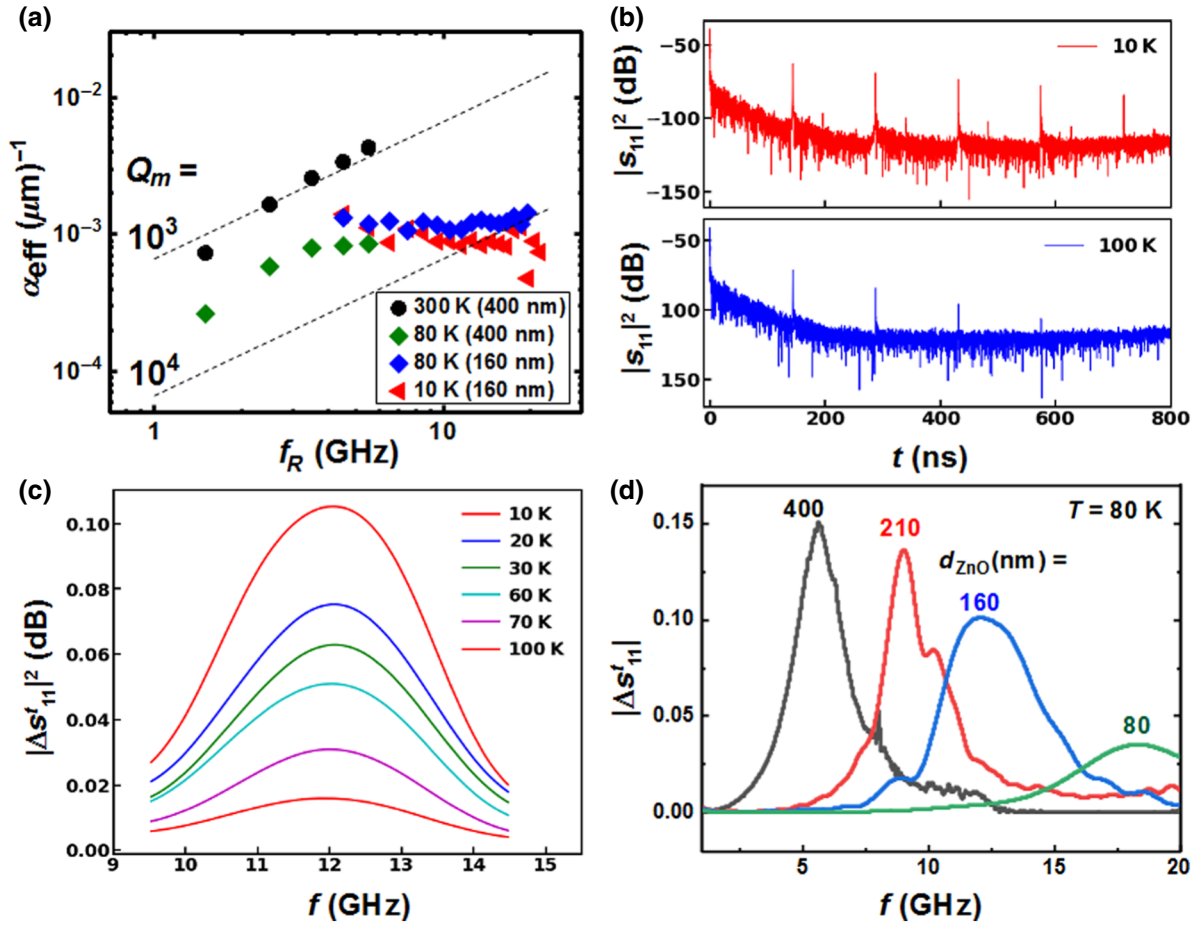
FIG. 7.   (a) The frequency dependence of the LBAW absorption coefficient α_{eff} at different temperatures. The dashed line shows the frequency dependence of α_{eff} required to yield the indicated quality factors Q_M defined in Eq. (6). (b) The impulse response of a BAWR with a (135 ± 5)-nm-thick ZnO layer (an active area of 490 μm^2) recorded at 10 K and 100 K. The time-domain traces are determined from s_{11} spectra recorded over a 6-GHz band around the resonance frequency $f_R = 12$ GHz. (c) The temperature dependence of the $|\Delta s_{11}^t|^2$ response for a BAWR with $f_R = 12$ GHz (the temperatures are listed in the legend). (d) $|\Delta s_{11}^t|^2$ spectra recorded at 80 K for BAWRs fabricated with different ZnO layer thicknesses d_{ZnO}.

For both BAWRs in Fig. 8, the $|s_{11}|^2$ spectrum (solid curve) shows a minimum at f_R, with a much narrower half width than in Fig. 7(d). The difference arises from the fact that DBRs confine the vibrations in a region close to the BAWRs. As a result, vibrations produced at successive rf cycles interfere constructively, thus leading to a higher amplitude.

In order to determine the acoustic quality factor Q and the effective electromechanical coupling coefficient k_{eff}^2, we also show in Fig. 8 the admittance ($|y_{11}|$) spectra of the structures [37]. The latter display a maximum followed by a minimum corresponding to the serial and parallel resonance frequencies f_s and f_p, respectively. The dashed lines in Fig. 8(a) show the values for $|s_{11}|$ and $|y_{11}|$ obtained by fitting the experimental data to the modified BvD model of Fig. 6(d). From the values for the lumped-circuit components obtained from the fits, we determine the resonance frequencies $f_p = \left(2\pi \sqrt{L_a(C_a + C_s)/(C_a C_s)}\right)^{-1}$ and

$f_s = f_R = \left(2\pi \sqrt{L_a C_a}\right)^{-1}$ [37,38] and the quality factor

$$Q = \frac{1}{2}\frac{f_p + f_s}{f_p - f_s}, \qquad (3)$$

as well as the effective coupling coefficient

$$k_{\text{eff}}^2 = \frac{\pi}{2}\frac{f_s}{f_p} \tan\left(\frac{\pi}{2}\frac{f_s}{f_p}\right) \qquad (4)$$

for the sample in (a), following the procedure described in Ref. [37]. We obtain $k_{\text{eff}}^2 = 1.1\%$ as well as a quality factor $Q = 360$. The latter is most likely determined by leakage of the LBAW into the substrate due to the finite thickness of the DBR rather than by acoustic absorption within the DBR region.

The 19.6-GHz sample in Fig. 8(b) has a narrower $|s_{11}|^2$ resonance, which is probably due to the larger number of
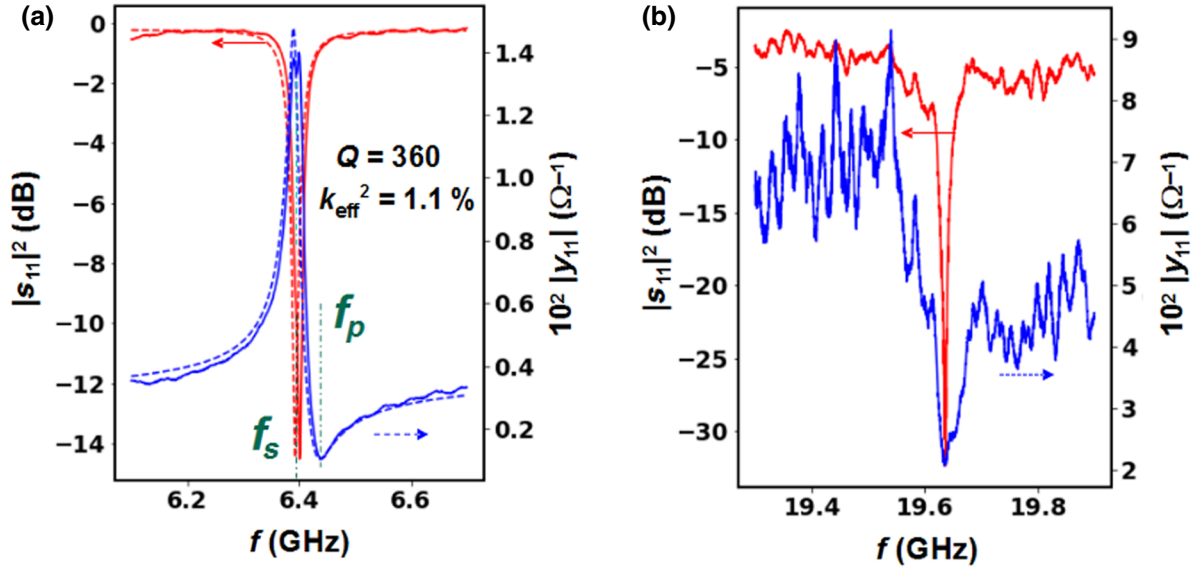
FIG. 8. The electric response at 10 K of BAWRs with resonant frequencies of (a) 6.4 GHz and (b) 19.64 GHz deposited on (Al,Ga)As distributed Bragg reflectors (DBRs). The solid (red) and dashed (blue) curves display the measured and fitted values to the $|s_{11}|^2$ (left-hand scale) and $|y_{11}|$ spectra, respectively. The fits are carried out to the BvD model of Fig. 6(d). The nominal ZnO thicknesses in (a) and (b) are 440 nm and 70 nm, respectively. f_s and f_p in (a) denote the serial and parallel resonance frequencies of the structures used to determine the quality factor Q and the effective coupling coefficient k_{eff}^2.

DBR pairs and, therefore, reduced wave leakage to the substrate. Its $|s_{11}|^2$ response has, however, a higher baseline (approximately -5 dB) than that for the 6.4-GHz sample. In addition, the fitting procedure used before cannot be reliably applied to extract the Q factor and the electromechanical coupling k_{eff}^2. The reasons for this behavior are currently under investigation.

IV. LBAW ABSORPTION IN GAAS

The results of the previous sections set the base for the piezoelectric generation of SHF LBAWs in GaAs. In this section, we turn our attention to the mechanisms determining the damping of LBAWs in GaAs in the SHF range as well as to the consequences for high-quality acoustic resonators operating in this range.

A. Quality factor and acoustic absorption mechanisms

The temperature and frequency dependencies of α_{eff} are summarized by the symbols in Fig. 7(a). At room temperature, the effective absorption follows a power-law dependence $\alpha_{\text{eff}} \sim f^m$, with an exponent m between 1 and 2. At low temperatures, in contrast, α_{eff} becomes essentially independent of frequency within the investigated frequency range, thus yielding an exponent $m \sim 0$.

Assuming that the LBAWs propagate with the GaAs longitudinal velocity v_{GaAs}, α_{eff} becomes related to the

BAW decay time τ_p according to the following equation:

$$\tau_p = \frac{1}{2\alpha_{\text{eff}} v_{\text{GaAs}}}. \tag{5}$$

The factor of 2 in the denominator accounts for the fact that τ_p is defined as an energy- (rather than amplitude-) loss rate. Using Eq. (5), we obtain the following expression for the upper limit Q_M for the quality factor of a GaAs acoustic resonator operating at frequency f_R [39]:

$$Q_M = \frac{f_R}{\Delta f_R} = 2\pi f_R \tau_p = \frac{\pi}{v_{\text{GaAs}}} \frac{f_R}{\alpha_{\text{eff}}}. \tag{6}$$

The dashed lines in Fig. 7(a) show the expected frequency dependence of α_{eff} required for achieving the quality factors Q_M indicated in the figure. Due to the exponent $m > 1$ in the frequency dependence of α_{eff} at room temperature, Q_M is expected to decrease with increasing f_R. For low temperatures, in contrast, $m \sim 0$ and we reach the favorable situation in which the contribution to quality factor associated with acoustic absorption reduces with increasing f_R.

To address the mechanisms responsible for acoustic absorption α_{eff} for propagating LBAWs in the GaAs, we summarize in Fig. 9(a) the measured temperature dependence of α_{eff} for LBAW with different frequencies. In all cases, α_{eff} exhibits a flat region at low temperatures followed by a second region with an approximately
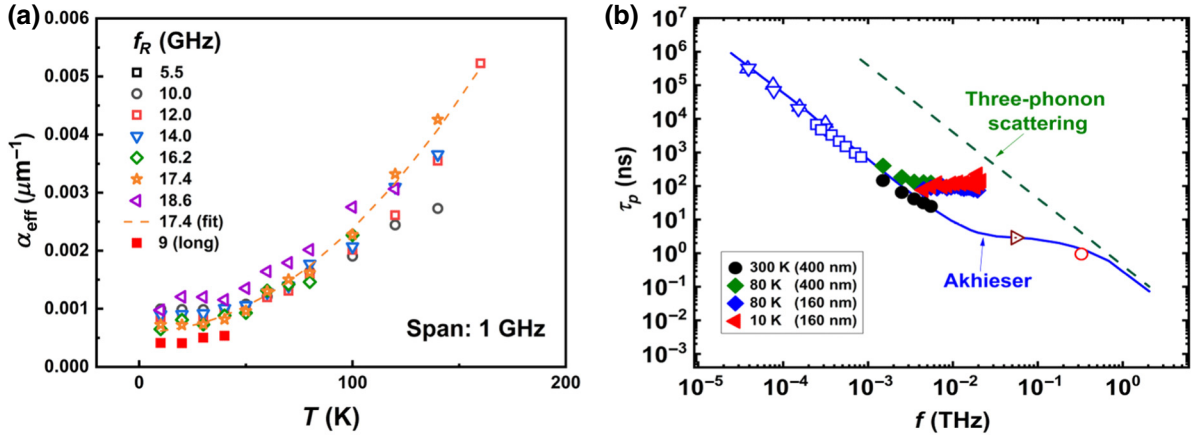
FIG. 9. (a) The temperature dependence of α_{eff} measured in BAWRs with different resonance frequencies f_R. The dashed line is a parabolic fit to the data for $f_R = 17.4$ GHz [cf. Eq. (6)]. (b) The frequency dependence of the LBAW lifetime τ_p. The solid symbols show the results from the present studies for different temperatures. The open symbols for frequencies below 1 GHz display measured results obtained by ultrasound-propagation studies along the GaAs $\langle 100 \rangle$ (downward triangles, Ref. [20]) and $\langle 111 \rangle$ directions (upward triangles, Ref. [20]; open squares, Ref. [22]). The open circle and right-facing triangle are laser picosecond results from Refs. [23] and [24]. The solid and dashed lines are the predictions from the Akhieser and three-phonon model from Ref. [24], respectively.

quadratic dependence on temperature. This behavior can be summarized by the following expression:

$$\alpha_{\mathrm{eff}}(f,T) = \alpha_{\mathrm{eff},0}(f) + \alpha_{\mathrm{eff},1}(f)\left[\frac{T}{300\ \mathrm{K}}\right]^2. \quad (7)$$

Here, $\alpha_{\mathrm{eff},0}$ is the saturation value of the absorption at low temperatures, while $\alpha_{\mathrm{eff},1}$ denotes the coefficient of the temperature-dependent term T^2. The dashed line in Fig. 9(a) is a fit of Eq. (7) to the data for the $f_R = 17.4$ GHz structure yielding $\alpha_{\mathrm{eff},0} = 6 \times 10^{-4}\ \mu\mathrm{m}^{-1}$ and $\alpha_{\mathrm{eff},1} = 0.016\ \mu\mathrm{m}^{-1}$.

The effective coefficient $\alpha_{\mathrm{eff}}(f)$ can also be expressed as a sum of contributions from different loss mechanisms according to the following equation:

$$\alpha_{\mathrm{eff}} \cong \alpha_{\mathrm{prop}} + \frac{1}{d_{\mathrm{GaAs}}}[\ln r_{\mathrm{TS}} + \ln r_{\mathrm{BS}} + \ln r_e + \ln r_{\mathrm{misc}}]. \quad (8)$$

To simplify the notation, we omit the functional dependence of the different terms of Eq. (8) on frequency and temperature. In this equation, α_{prop} gives the intrinsic absorption losses of the LBAW during propagation through both the BAWR and the GaAs substrate. The terms within the square brackets account for losses due to surfaces, interfaces, and beam diffraction. r_{BS} denotes the losses due to reflection at the bottom surface as well as leakage to the underlying sample holder. The latter depend on the surface roughness as well as on the acoustic coupling to the underlying medium. The term r_{TS} quantifies the effective losses during the propagation through the BAWR as well as scattering at its surface and interfaces,

while r_e accounts for the acoustic losses per round trip due to the electroacoustic conversion within the BAWR. The last term, r_{misc}, encompasses additional loss mechanisms, such as diffraction, nonparallelism of the wafer surfaces, etc.

B. Acoustic losses at room temperature

Except for the first contribution, α_{prop}, all terms on the right-hand side of Eq. (8) are expected to be weakly temperature dependent, thus indicating that this term dominates at room temperature. Furthermore, since the wave-propagation distance within the BAWRs is over 3 orders of magnitude shorter than in the GaAs substrate, we will assume that propagation losses within the BAWR are smaller than in the substrate (for this reason, in Eq. (8) we use the substrate thickness d_{GaAs} rather than the total sample thickness). Consequently, the temperature-dependent contribution in Eq. (7), which dominates the losses at room temperature, must thus be related to the intrinsic LBAW absorption during propagation through the GaAs substrate. In fact, several LBAW-propagation studies in GaAs have reported a quadratic dependence of α_{eff} like the one in Eq. (7). The measured coefficients $\alpha_{\mathrm{eff},1}(f)$ range from 0.04 $\mu\mathrm{m}^{-1}$ for 56-GHz LBAWs [23] to 0.25 $\mu\mathrm{m}^{-1}$ for 713-GHz waves [40]. The value $\alpha_{\mathrm{eff},1}(f) = 0.016\ \mu\mathrm{m}^{-1}$ determined in Sec. IV A for frequencies between 5 and 20 GHz follows this trend with frequency, as well. Such a dependence has been associated with the interaction of the LBAW with thermal phonons.

Figure 9(b) compares the LBAW lifetime $\tau_p = 1/(2\alpha_{\mathrm{eff}}v_{\mathrm{GaAs}})$ (as previously mentioned, the factor of 2

arises from the fact that τ_p is defined as an intensity decay time) obtained in the present studies at different temperatures (solid symbols) with previously reported data (adapted from Fig. 4 of Ref. [24]). The data below 1 GHz were determined by ultrasound absorption while points above 50 GHz were obtained using laser acoustics. The SHF LBAW propagation studies reported here cover the frequency window for the acoustic absorption of LBAW modes from 1 to 20 GHz, which has so far not been experimentally accessed in GaAs. The solid and dashed lines in Fig. 9(b) are the predictions of the Akhieser and three-phonon models, respectively [24]. These models describe the mechanism of LBAW damping associated with the interaction with high-frequency thermal phonons. Note that our present data set for room temperature (filled circles) is fully consistent with previous experimental results as well as with the predictions of the Akhieser model. According to this model, the strain field of the LBAW changes the energy distribution of thermal phonons via the Grüneisen parameters. The thermal vibrations readjust their energy distribution via anharmonic effects on a time scale that is short in comparison with the LBAW period, thus leading to an irreversible energy transfer to the thermal bath [41,42].

C. Acoustic losses at low temperatures

At low temperatures, the acoustic absorption reduces significantly and saturates at a frequency-dependent value $\alpha_{\mathrm{eff},0}$ (cf. Fig. 9). The latter is expected to be determined by the second term on the right-hand side of Eq. (8). In order to identify the mechanisms responsible for acoustic losses at low temperatures, we perform two additional control experiments. The first one addresses losses associated with reflections at the back surface (r_{BS}) as well as with leakage to the underlying sample holder. For that purpose, we measure α_{eff} at room temperature for a BAWR with $f_R = 5$ GHz under different mounting conditions: (i) suspended, (ii) in contact with the substrate holder, and (iii) glued to the substrate holder. The changes in α_{eff} are of less than 10% and, thus, smaller than $\alpha_{\mathrm{eff},0}$ in Fig. 7(a). This result indicates that this mechanism plays a minor role in the propagation losses at room temperature. These experimental studies, however, cannot be extended to low temperatures.

In a second set of experiments, we carry out acoustic absorption measurements at low temperatures over much longer propagation distances d_{GaAs}. As can be inferred from Eq. (8), a larger d_{GaAs} increases the relative weight of the intrinsic absorption (first term on the right-hand side) over the other terms, thus indirectly yielding information about the role of surfaces and interfaces. The experiments are carried out by exciting LBAWs using BAWRs fabricated on a (110) GaAs slab. The substrates are from the same batch as those used for the previous studies,

but the LBAWs now propagate along the ⟨110⟩ direction. In addition, while the upper and bottom surfaces of the (100) GaAs wafers are polished, those of the (110) GaAs slabs are cleaved, which may result in different acoustic reflection properties.

The solid squares in Fig. 9(a) show the effective absorption coefficient measured on a 1.5-μm-thick ⟨110⟩ GaAs slab. Due to the thicker substrates, the echo propagation lengths in these samples are approximately 4 times longer than in the previous experiments. Interestingly, α_{eff} reduces by a factor of approximately 2 as compared to the results obtained for shorter propagation lengths. It is unlikely that the reduced absorption results from differences in propagation direction: in fact, previous studies have reported similar damping coefficients for LBAW propagation along the ⟨100⟩ and ⟨111⟩ directions [see, e.g., the results from Ref. [20] displayed in Fig. 9(b)]. Furthermore, the reduced absorption with longer propagation lengths also enables us to discard phonon diffraction as a loss mechanism. Rather, we assign the lower α_{eff} to the reduced role of losses at interfaces and surfaces in the longer samples. The role of surface defects has been highlighted in recent studies of the absorption losses of acoustic resonators at low temperatures [43,44]. As an important consequence, the present results show that the acoustic absorption at low temperatures is limited by extrinsic (rather than by intrinsic) mechanisms, which can be minimized by improving the quality of the surfaces and interfaces.

V. CONCLUSIONS

We demonstrate the feasibility of piezoelectric generation of LBAWs in GaAs crystals with frequencies up to 20 GHz. The LBAWs are excited using BAWRs based on a thin ZnO layer produced by rf sputtering as a piezoelectric medium. The BAWRs are fabricated using a simple process that combines the evaporation and sputtering through a shadow mask to define the lateral dimensions of the bottom contact and ZnO film, respectively, with the photolithographic fabrication of the top contact, which defines the active area of the structures. We show that the structural properties of the ZnO layers, as well as the electroacoustic conversion efficiency of the BAWRs, depend sensitively on the sputtering conditions of the ZnO films. Finally, we demonstrate that by reducing the thickness of the ZnO film, we can increase the resonance frequency of the structures up to 19.6 GHz.

The electroacoustic properties of the BAWRs are probed by rf reflection measurements in the frequency and time domains. BAWRs deposited directly on GaAs substrates exhibit low (30–40%) electroacoustic power-conversion efficiency, which is mainly limited by the large impedance mismatch between the electric and acoustic loads. Significantly higher conversion efficiencies are achieved on structures fabricated on an acoustic DBR. By recording

the acoustic echoes created by reflections at the sample boundaries, we develop a procedure to (i) measure the LBAW propagation losses with very high accuracy and (ii) determine the absolute electroacoustic conversion efficiency into a LBAW. The SHF BAWRs enable us to measure the acoustic absorption coefficient α_{eff} with high accuracy in the previously unexplored frequency range from 1 to 20 GHz. The acoustic absorption coefficient measured at room temperature agrees very well with the predicted dependence expected from the interaction with thermal phonons. Since the inverse of the LBAW lifetime increases superlinearly with frequency, the quality factor of acoustic resonators on GaAs reduces with frequency. As the temperature decreases, the absorption saturates at a frequency-dependent value, which appears to be determined by scattering at surfaces and interfaces. Due to the weak frequency dependence of the absorption at low temperatures, the quality factors of resonators should increase with frequency, thus becoming an important consideration for the development of SHF resonators. Furthermore, the dependence of the acoustic absorption at low temperatures with the propagation length shows that the losses are not of intrinsic character and can, thus, be minimized by proper design and control of the device interfaces. The present studies thus pave the way for the realization of high-quality nanomechanical resonators operating in the SHF range as well as for use of these vibrations for the modulation and control of semiconductor nanostructures.

ACKNOWLEDGMENTS

[1] P. Delsing *et al.*, The 2019 surface acoustic waves roadmap, J. Phys. D **52**, 353001 (2019).

[2] R. M. White, in *Proc. of the IEEE* (IEEE, New York, 1970), Vol. 58, p. 1238.

[3] B. A. Auld, *Acoustic Fields and Waves in Solids* (Robert E. Krieger Publishing Company, Inc., Malabar, Florida, 1990).

[4] D. Royer and E. Dieulesaint, *Elastic Waves in Solids I* (Springer, Berlin, 2000).

[5] M. Aspelmeyer, T. J. Kippenberg, and F. Marquardt, Cavity optomechanics, Rev. Mod. Phys. **86**, 1391 (2014).

[6] A. D. O'Connell, M. Hofheinz, M. Ansmann, R. C. Bialczak, M. Lenander, E. Lucero, M. Neeley, D. Sank, H. Wang, M. Weides, J. Wenner, J. M. Martinis, and A. N. Cleland, Quantum ground state and single-phonon control of a mechanical resonator, Nature **464**, 697 (2010).

[7] M. Gustafsson, P. V. Santos, G. Johansson, and P. Delsing, Local probing of propagating acoustic waves in a gigahertz echo chamber, Nat. Phys. **8**, 338 (2012).

[8] K. J. Satzinger, Y. P. Zhong, H.-S. Chang, G. A. Peairs, A. Bienfait, M.-H. Chou, A. Y. Cleland, C. R. Conner, É. Dumur, J. Grebel, I. Gutierrez, B. H. November, R. G. Povey, S. J. Whiteley, D. D. Awschalom, D. I. Schuster, and A. N. Cleland, Quantum control of surface acoustic-wave phonons, Nature **563**, 661 (2018).

[9] W. J. M. Naber, T. Fujisawa, H. W. Liu, and W. G. van der Wiel, Surface-Acoustic-Wave-Induced Transport in a Double Quantum Dot, Phys. Rev. Lett. **96**, 136807 (2006).

[10] M. Metcalfe, S. M. Carr, A. Muller, G. S. Solomon, and J. Lawall, Resolved Sideband Emission of InAs/GaAs Quantum Dots Strained by Surface Acoustic Waves, Phys. Rev. Lett. **105**, 037401 (2010).

[11] O. D. D. Couto, Jr., S. Lazić, F. Iikawa, J. Stotz, R. Hey, and P. V. Santos, Photon anti-bunching in acoustically pumped quantum dots, Nat. Phot. **3**, 645 (2009).

[12] D. A. Golter, T. Oo, M. Amezcua, K. A. Stewart, and H. Wang, Optomechanical Quantum Control of a Nitrogen-Vacancy Center in Diamond, Phys. Rev. Lett. **116**, 143602 (2016).

[13] M. Weiler, L. Dreher, C. Heeg, H. Huebl, R. Gross, M. S. Brandt, and S. T. B. Goennenwein, Elastically Driven Ferromagnetic Resonance in Nickel Thin Films, Phys. Rev. Lett. **106**, 117601 (2011).

[14] M. Rinaldi, C. Zuniga, Z. Chengjie, and G. Piazza, Super-high-frequency two-port AlN contour-mode resonators for rf applications, IEEE Trans. Ultrason., Ferroelectr., Freq. Control **57**, 38 (2010).

[15] H. P. Loebl, M. Klee, C. Metzmacher, W. Brand, R. Milsom, and P. Lok, Piezoelectric thin AlN films for bulk acoustic wave (BAW) resonators, Mater. Chem. Phys. **79**, 143 (2003).

[16] R. Lanz and P. Muralt, in *IEEE Symposium on Ultrasonics, 2003* (IEEE, Piscataway, 2003), Vol. 1, p. 178.

[17] K. Umeda, H. Kawamura, M. Takeuchi, and Y. Yoshino, Characteristics of an AlN-based bulk acoustic wave resonator in the super high frequency range, Vacuum **83**, 672 (2008), selected Papers revised from the Proceedings of the Ninth International Symposium on Sputtering and Plasma Processes (ISSP 2007), 6–8 June 2007, Kanazawa, Japan.

[18] I. V. Kukushkin, J. H. Smet, L. Höppel, U. Waizmann, M. Riek, W. Wegscheider, and K. von Klitzing, Ultrahigh-frequency surface acoustic waves for finite wave-vector spectroscopy of two-dimensional electrons, Appl. Phys. Lett. **85**, 4526 (2004).

[19] S. Büyükköse, B. Vratzov, J. van der Veen, P. V. Santos, and W. G. van der Wiel, Ultrahigh-frequency surface acoustic wave generation for acoustic charge transport in silicon, Appl. Phys. Lett. **102**, 013112 (2013).

[20] R. I. Cottam and G. A. Saunders, Ultrasonic attenuation in GaAs from 2 K to 300 K, J. Phys. C: Solid State Phys. **7**, 2447 (1974).

[21] R. Legrand, A. Huynh, B. Jusserand, B. Perrin, and A. Lemaître, Direct measurement of coherent subterahertz acoustic phonons mean free path in GaAs, Phys. Rev. B **93**, 184304 (2016).

[22] S. Ivanov, J. M. Kotelyanskii, G. D. Mansfeld, and E. N. Khazanov, Nonlinear effects in the propagation of hypersonic waves in indium antimonide, Sov. Phys. Solid State **13**, 508 (1971).

[23] W. Chen, H. J. Maris, Z. R. Wasilewski, and S.-I. Tamura, Attenuation and velocity of 56 GHz longitudinal phonons in gallium arsenide from 50 to 300 K, Philos. Mag. B **70**, 687 (1994).

[24] A. A. Maznev, F. Hofmann, A. Jandl, K. Esfarjani, M. T. Bulsara, E. A. Fitzgerald, G. Chen, and K. A. Nelson, Lifetime of sub-THz coherent acoustic phonons in a GaAs-AlAs superlattice, Appl. Phys. Lett. **102**, 041901 (2013).

[25] U. Kaletta, P. V. Santos, D. Wolansky, A. Scheit, M. Fraschke, C. Wipf, P. Zaumseil, and C. Wenger, Monolithic integrated SAW-filter based on AlN for high-frequency applications, Semicond. Sci. Technol. **28**, 065013 (2013).

[26] D. Machado *et al.*, Private commun.

[27] J. Gualtieri, J. Kosinski, and A. Ballato, Piezoelectric materials for acoustic wave applications, IEEE Trans. Ultrason. Ferroelectr. Freq. Control **41**, 53 (1994).

[28] P. Dular, C. Geuzaine, F. Henrotte, and W. Legros, A general environment for the treatment of discrete problems and its application to the finite element method, IEEE Trans. Magn. **34**, 3395 (1998).

[29] A. Hernández-Mínguez, Y.-T. Liou, and P. V. Santos, Interaction of surface acoustic waves with electronic excitations in graphene, J. Phys. D: Appl. Phys. **51**, 383001 (2018).

[30] R. Wagers, G. Kino, P. Galle, and D. Winslow, in *1972 Ultrasonic Symposium* (IEEE, Piscataway, 1972), p. 194.

[31] M. Yuan, C. Hubert, S. Rauwerdink, A. Tahraoui, B. van Someren, K. Biermann, and P. V. Santos, Generation of surface acoustic waves on doped semiconductor substrates, J. Phys. D **50**, 484004 (2017).

[32] O. Madelung, U. Rössler, and M. Schulz, eds., *Gallium Arsenide (*GaAs*) Sound Velocities, Ultrasonic Attenuation, Phonon Viscosity: Datasheet from Landolt-Börnstein—Group III Condensed Matter. Vol. 41A1α: "Group IV Elements, IV–IV and III–V Compounds. Part A—Lattice Properties"* in *Springer Materials* (Springer-Verlag, Berlin, 1983), p. 41.

[33] J. D. Larson III, P. D. Bradley, S. Wartenberg, and R. C. Ruby, in *IEEE Ultras. Symp.* (IEEE, Piscataway, 2000), p. 863.

[34] W. E. Newell, Face-mounted piezoelectric resonators, Proc. IEEE **53**, 575 (1965).

[35] K. M. Lakin, K. T. McCarron, and R. E. Rose, in *1995 IEEE Ultrasonics Symposium. Proceedings. An International Symposium* (IEEE, Piscataway, 1995), Vol. 2, p. 905.

[36] M. Trigo, A. Bruchhausen, A. Fainstein, B. Jusserand, and V. Thierry-Mieg, Confinement of Acoustical Vibrations in a Semiconductor Planar Phonon Cavity, Phys. Rev. Lett. **89**, 227402 (2002).

[37] K. Hashimoto, in *RF Bulk Acoustic Wave Filters for Communications*, edited by K. ya Hashimoto (Artech House Microwave Library, Boston, London, 2009).

[38] J. V. Tirado, Ph.D. thesis, Universitat Autònoma de Barcelona, (2010).

[39] B. C. Daly, K. Kang, Y. Wang, and D. G. Cahill, Picosecond ultrasonic measurements of attenuation of longitudinal acoustic phonons in silicon, Phys. Rev. B **80**, 174112 (2009).

[40] M. Markov, J. Sjakste, N. Vast, R. Legrand, B. Perrin, and L. Paulatto, Breakdown of Herring's processes in cubic semiconductors for subterahertz longitudinal acoustic phonons, Phys. Rev. B **98**, 245201 (2018).

[41] H. Maris, in *Physical Acoustics*, edited by W.P. Mason (Academic Press, New York, 1971), Vol. 8, p. 279.

[42] J.-Y. Duquesne and B. Perrin, Ultrasonic attenuation in a quasicrystal studied by picosecond acoustics as a function of temperature and frequency, Phys. Rev. B **68**, 134205 (2003).

[43] R. Manenti, M. J. Peterer, A. Nersisyan, E. B. Magnusson, A. Patterson, and P. J. Leek, Surface acoustic wave resonators in the quantum regime, Phys. Rev. B **93**, 041411 (2016).

[44] M. Hamoumi, P. E. Allain, W. Hease, E. Gil-Santos, L. Morgenroth, B. Gérard, A. Lemaître, G. Leo, and I. Favero, Microscopic Nanomechanical Dissipation in Gallium Arsenide Resonators, Phys. Rev. Lett. **120**, 223601 (2018).